Geophysical Research Letters

RESEARCH LETTER
10.1029/2020GL091248

The Seasonality of Global Land and Ocean Mass and the Changing Water Cycle

Hrishikesh A. Chandanpurkar[1], John T. Reager[1], James S. Famiglietti[2,3], R. Steven Nerem[4,5,6], Don P. Chambers[7], Min-Hui Lo[8], Benjamin D. Hamlington[1], and Tajdarul H. Syed[9]

[1]Jet Propulsion Laboratory, California Institute of Technology, Pasadena, CA, USA, [2]Global Institute for Water Security, University of Saskatchewan, Saskatoon, SK, Canada, [3]School of Environment and Sustainability, University of Saskatchewan, Saskatoon, SK, Canada, [4]Colorado Center for Astrodynamics Research, University of Colorado, Boulder, CO, USA, [5]Ann and H. J. Smead Department of Aerospace Engineering Sciences, University of Colorado, Boulder, CO, USA, [6]Cooperative Institute for Research in Environmental Sciences, University of Colorado, Boulder, CO, USA, [7]College of Marine Science, University of South Florida, St. Petersburg, FL, USA, [8]Department of Atmospheric Sciences, National Taiwan University, Taipei, Taiwan, [9]Department of Earth Sciences, Indian Institute of Technology Kanpur, Kanpur, India

Key Points:

- The seasonal amplitude of global ocean and land water mass describes the seasonal global water cycle and is a metric of its strength
- The seasonal amplitude varies interannually with magnitude comparable to the long-term trend in global ocean mass
- Hydrological changes in specific land regions are most responsible for these year-to-year variations

Correspondence to:
J. S. Famiglietti,
james.famiglietti@usask.ca

Citation:
Chandanpurkar, H. A., Reager, J. T., Famiglietti, J. S., Nerem, R. S., Chambers, D. P., Lo, M.-H., et al. (2021). The seasonality of global land and ocean mass and the changing water cycle. *Geophysical Research Letters*, *48*, e2020GL091248. https://doi.org/10.1029/2020GL091248

Received 15 OCT 2020
Accepted 14 MAR 2021

Abstract The global water cycle is generally viewed as the cycling of water masses among the land, ocean, and atmosphere. This cycling predominantly occurs at the annual time scale and between land and ocean, constituting the seasonal global water cycle. NASA's Gravity Recovery and Climate Experiment (GRACE) and GRACE-Follow On missions can directly observe the seasonal global water cycle and describe the changes in its intensity. We present seasonal amplitudes of the global land water and ocean mass anomalies between 04/2002 and 11/2020. We find that the average seasonal amplitude is 17.0 ± 0.6 mm sea level equivalent (SLE), and its interannual variability (σ = 1.1 mm SLE) is comparable to the long-term trends in the land and ocean masses. We investigate two periods of rapid amplification and deamplification during which the amplitude changed as much as 29%, and find that changes in hydroclimatology in certain land regions modulate the seasonal global water cycle.

Plain Language Summary The global water cycle is generally viewed as the cycling of water among the land, ocean, and atmosphere. By observing the changes in the water mass, NASA's Gravity Recovery and Climate Experiment (GRACE) and GRACE-Follow On missions are capable of measuring the global water cycle, and its changes, directly. The largest portion of the cycling occurs between global land and global ocean at the annual time scale, constituting the seasonal global water cycle. We present the amplitude of this cycling, its year-to-year changes that describe the changes in the intensity of the seasonal global water cycle, and the regions contributing to it.

1. Mass Changes in Global Water Storages

Between 04/2002 and 06/2017, the Gravity Recovery and Climate Experiment (GRACE) satellite mission (Tapley et al., 2019) provided the opportunity to monitor integrated water mass changes in Earth's four major water reservoirs: land (e.g., Reager et al., 2016), ocean (e.g., Cazenave et al., 2018; Chambers et al., 2017), and the two ice sheets (e.g., Mouginot et al., 2019; Shepherd et al., 2018). The GRACE-Follow On (GRACE-FO) mission continues to monitor these water mass changes since 06/2018 (e.g., Velicogna et al., 2020). These observations have improved our understanding of interannual variability and long-term changes in water mass anomalies across these major reservoirs. Figure 1 shows the time series of the four reservoirs. During 04/2002–11/2020, Greenland, Antarctica, and the global land lost water mass at the rate of 0.76 ± 0.02, 0.39 ± 0.02, and 0.87 ± 0.06 mm sea level equivalent (SLE)/year respectively, which contributed to an overall increase in global ocean mass at the rate of 2.02 ± 0.07 mm SLE/year (trend uncertainties are described in Section 2.3). The increase in global ocean mass is responsible for more than half of the ~3.3 mm/year observed increase in the global mean sea level (GMSL) (Cazenave et al., 2018; Hamlington et al., 2020; https://sealevel.nasa.gov/).

Unlike the Greenland and Antarctica ice sheets, global land and global ocean water mass anomalies exhibit a pronounced seasonal cycle (at about 1-year frequency, also referred to in the literature as the "annual

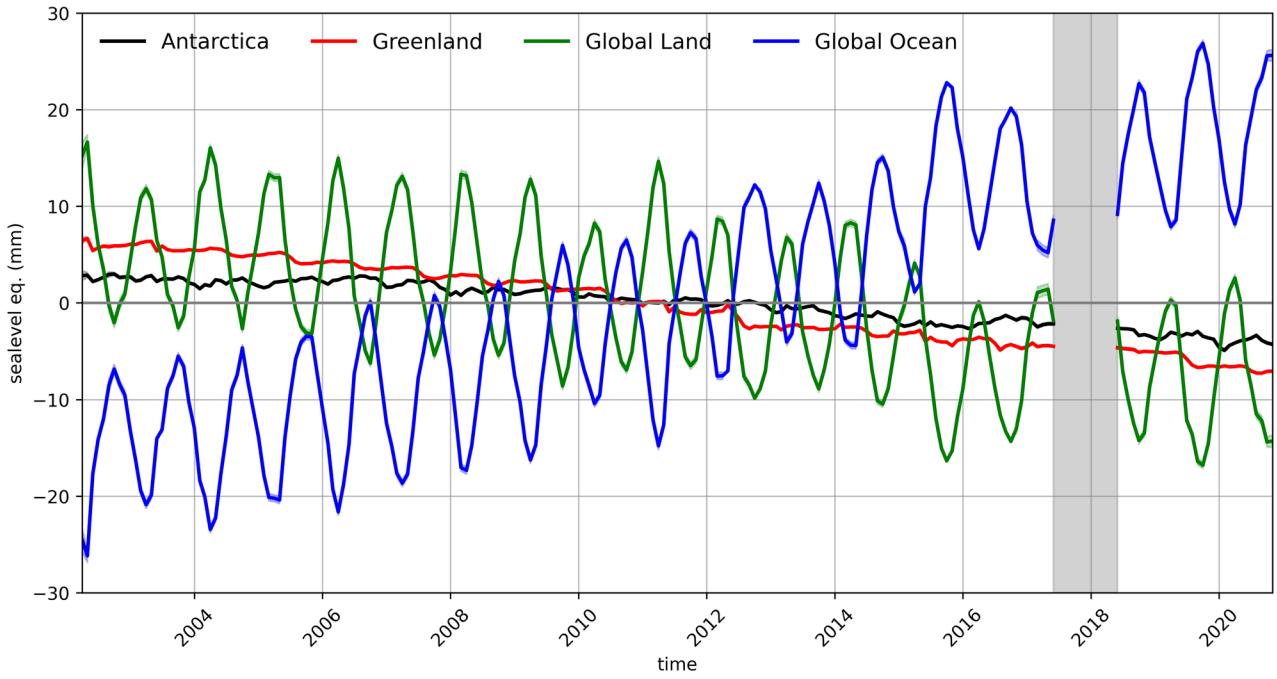

Figure 1. Water mass anomalies in Earth's four major water storages from Gravity Recovery and Climate Experiment (GRACE) and GRACE-Follow On (GRACE-FO) missions. The shaded areas denote 1-sigma uncertainty on the mass time series, computed from measurement errors provided with the mascon solution and leakage error correction following Wiese et al. (2016). The gray vertical band denotes the gap between the two missions.

cycle"). Since mass is conserved globally, the atmosphere's storage of water mass is negligibly less than that over land and ocean, and the contribution from the ice sheets at this time scale is negligible, the seasonal cycle over the ocean is nearly the exact opposite of that over land (i.e., one's gain is the other's loss, Figure 2a). In other words, at seasonal time scales, anomalies of global land water and global ocean masses can be thought to describe the seasonal global water cycle.

Studying the seasonal global water cycle is important, since the majority of the seasonal variations in GMSL comes from that in the global ocean mass (Chen et al., 1998; Willis et al., 2008). However, compared to long-term trends and interannual variability in ocean and land water masses, relatively few studies have focused on whether the seasonal cycle has changed. A likely reason for this is a long-held assumption that the seasonal cycle is time-invariant, that is, it stays constant from year-to-year. In the projections of future GMSL changes, the seasonal variability (and to a certain extent, interannual variability as well) is seen as a time-invariant envelope on the underlying trend projections that play a key role in coastal flooding, especially when combined with local aspects such as tides and storm surges. However, in a regional-scale study, Hamlington et al. (2019) recently showed that the seasonality in water mass over most land regions varies from year-to-year, modulated by interannual to decadal climate variability. Hence, understanding the changes in the seasonal water cycle at a global scale is likely to have implications on designing such envelopes on the future GMSL projections.

Variations in the seasonal amplitude of global ocean and land have broader implications than just GMSL budgets, as they describe fundamental changes in the intensity of seasonal global water cycle (Figure 2b). Globally, the water cycle is expected to intensify in response to anthropogenic climate change. However, most literature on water cycle intensification focuses on regional changes in hydrologic fluxes such as precipitation, evapotranspiration, and runoff, and often on the long-term trends in these quantities (Dirmeyer & Brubaker, 2007; Held & Soden, 2006; Huntington, 2006; Lan et al., 2019; Peterson et al., 2002; Syed et al., 2007; Trenberth et al., 2007; Walter et al., 2004). However, considering that the largest amount water cycling predominantly occurs at the seasonal time scale, an amplification of the seasonal global water cycle can be one of the ways the water cycle intensification manifests (Figure 2b). This is supported by recent studies by Wu et al. (2015) and Liang et al. (2020). Wu et al. (2015) highlighted that the seasonal variations

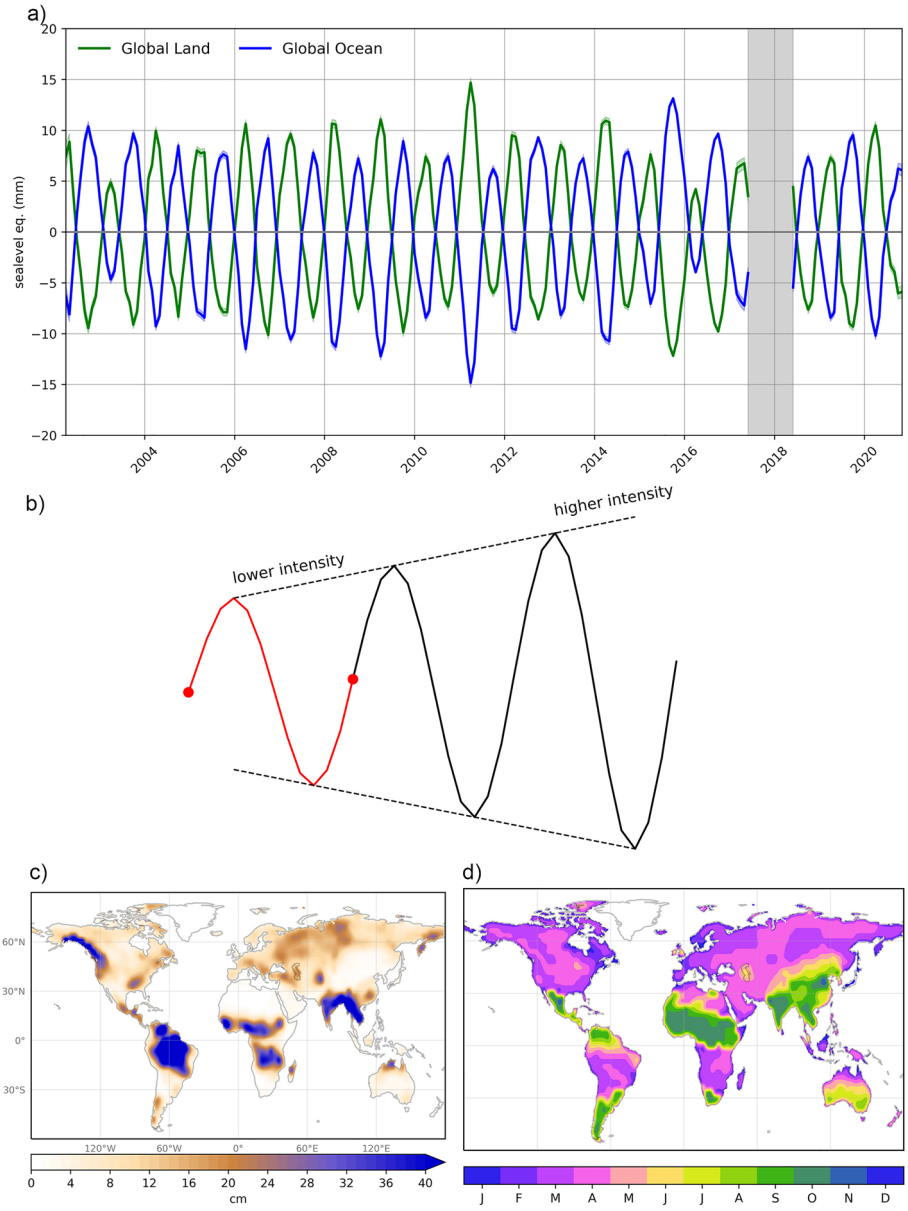

Figure 2. (a) Detrended spatially integrated water mass anomalies over global land and global ocean. (b) Schematic representation of increase (or decrease) in the seasonal amplitude of global land water and ocean mass suggesting higher (or lower) intensity of the seasonal global water cycle. (c) Trough-to-peak amplitude of annual harmonic of the land water mass anomalies in the units of water equivalent thickness (cm). (d) Month corresponding to the seasonal peak storage.

of the land water storage are expected to be stronger under global warming, while Liang et al. (2020) showed the increased seasonality of precipitation can affect the ocean's salinity variations within the Amazon river hydrological system. In this context, GRACE observations of the seasonal global water cycle could be a useful metric to measure the changes in the water cycle intensification. Additionally, they provide an opportunity to understand the regional drivers of these changes (Figure 2c and 2d and corresponding discussion in Section 3).

Here, we present the seasonal cycle of global land water and ocean mass anomalies from GRACE and GRACE-FO as a measure of the seasonal global water cycle. We provide the long-term mean trough-to-peak annual amplitude (seasonality), and the land regions that contribute the most to this global seasonal

amplitude. We then characterize variations in the global seasonal amplitude, focusing on two periods corresponding to its rapid increase and decrease, representing changes in the intensity of the seasonal global water cycle. Finally, we identify regions that contribute significantly to these changes and examine precipitation as a potential hydroclimatic driver.

2. Data and Methods

2.1. Global Land Water and Ocean Mass Time Series

The Jet Propulsion Laboratory (JPL) GRACE and GRACE-FO Release 06 Mascon version 2 (RL06Mv2) solution solves for monthly gravity field variations in terms of 4,551 equal-area 3° spherical cap mascons (Watkins et al., 2015; Wiese et al., 2016). It includes a Coastline Resolution Improvement (CRI) filter to separate land and ocean portions of water mass within each land/ocean mascon in a postprocessing step. Atmospheric water mass anomalies are removed from the data using pressure fields from reanalysis. The data are gridded on a 0.5° grid at monthly intervals. Data are accessed from the GRACE Tellus website (https://grace.jpl.nasa.gov/). For more details on how the mascon solution is derived and on performance metrics regarding the solution, please see Watkins et al. (2015) and Wiese et al. (2016).

The data at each grid point are then converted to volume by multiplying with the local surface area, and then to sea level equivalent (mm SLE) by dividing by the total global ocean surface area (Reager et al., 2016). The water mass anomalies are then separated into four major reservoirs of global ocean, global land, Greenland, and Antarctica, by applying appropriate regional masks provided by JPL along with the mascon solution. Finally, the time series are spatially integrated to produce global water mass anomaly time series from these four major water stores.

2.2. Seasonal Amplitude of the Global Land Water and Ocean Mass Time Series

To estimate the seasonal cycle of the global land water and ocean mass anomalies, we fit an annual harmonic over running 2-year sections of the time series, and consider the trough-to-peak amplitude of this signal. Choosing 2-year sections instead of 1-year sections allows for the annual cycle to vary slightly while minimizing interference from low-frequency variability (Hamlington et al., 2019). The fitting method involves solving a least square function that simultaneously solves for the optimal values for a linear trend and an annual harmonic. The fit function is as follows:

$$fn = a_0 + a_1 t + a_2 \cos\left(2\pi f t\right) + a_3 \sin\left(2\pi f t\right) \tag{1}$$

where

t = time
a_0 = intercept
a_1 = linear slope
a_2 = amplitude of the cosine component of annual harmonic
a_3 = amplitude of the sine component of annual harmonic
f = frequency of annual period (1/12 for monthly sampled data)

The trough-to-peak seasonal amplitude A (representing total water exchange within the year) is then obtained by

$$A = 2\sqrt{\left(a_2^2 + a_3^2\right)} \tag{2}$$

2.3. Uncertainties in Data and Methods

Uncertainties on individual water mass time series of global land, ocean, Greenland, and Antarctica, as shown in Figures 1 and 2a, are 1-sigma uncertainty on the water mass anomalies, computed from measurement errors provided with the mascon solution and leakage error correction from GRACE and GRACE-FO

following Wiese et al. (2016). Uncertainties on the linear trend estimates of the four reservoirs described in Section 1 are twice the standard errors on the respective ordinary least square fits, that is, the square roots of the diagonal of the covariance matrices of the regression coefficients. For an estimate of trend uncertainties on water mass changes of these reservoirs that account for observation uncertainties, please refer to Cazenave et al. (2018), Chambers et al. (2017), or the NASA Sea Level Change portal (https://sealevel.nasa.gov/).

Uncertainties on the seasonal amplitude time series are computed as follows. First, standard errors are obtained as the square root of the diagonal of the covariance matrix of the parameters estimated in Equation 1. Then, the individual standard errors for the cosine and sine parameters are summed following the standard error propagation method of root sum of squares. Finally, using the resultant standard error, 95% confidence values are computed following a two-tailed Student *t*-test after accounting for reduced degrees of freedom due to the four estimated parameters. These 95% confidence values are used in Figure 3 and in the text as representing the uncertainty on the seasonal amplitude. Between 04/2002 and 06/2017 GRACE records, there are 22 months of no data due to instrument issues, primarily in the beginning part of the mission (from 05/2002 to 07/2002) and after 01/2011 when the scientific instrument had to be turned off several times a year due to battery degradation (Tapley et al., 2019). Between 08/2002 and 12/2010, only 1 month was not observed (06/2003). The number of outages doubled after 2015, from approximately two per year between 01/2011 and 12/2014 to four per year after 01/2015–06/2017. There are 2 months of missing data in the GRACE-FO records. Partial harmonic fits are computed in the 2-year sections featuring all these GRACE and GRACE-FO missing data. The associated uncertainty values of the seasonal amplitude during these months are higher due to under sampling. From 07/2017 to 05/2018, there is a gap between GRACE and GRACE-FO. These intermission gap months are ignored in the analysis.

While the above-mentioned uncertainties do not take into account uncertainty in the data itself, we use stricter confidence values (95%, instead of the standard error that represent confidence values of 66%). Furthermore, as the amplitude and uncertainty are computed for each of the running 2-year sections, uncertainties on adjacent amplitude points (in Figure 3a) are correlated. The correlation aspect of these uncertainties is not removed when providing the uncertainty over the average seasonal amplitude, in order to keep it comparable with the uncertainty of individual sections. In this, we believe the uncertainties presented here are likely inflated.

Land precipitation data from Global Precipitation Climatology Project version 2.3 (GPCP, Adler et al., 2003) are explored as potential drivers of the changes in the seasonal amplitude of land water masses. The precipitation data are available at 2.5° grid at monthly intervals. These data are extracted over land regions and are subjected to the same procedure as described in Section 2.2 to obtain the seasonal amplitudes of land precipitation.

In Figures 3b–3e, we show local trends in seasonal amplitudes during the amplification and deamplification periods. Only those trends that are significant at 95% confidence intervals are considered. Since multiple significance tests are likely to increase the false discovery rate, a correction to the significance is applied following Benjamini and Hochberg (1995).

3. Results and Discussion

3.1. The Mean Amplitude of the Seasonal Global Water Cycle

The seasonal amplitudes of global land water and ocean mass anomalies are shown in Figure 3a. The two time series are highly correlated (correlation coefficient = 0.98), which is somewhat by design, since GRACE and GRACE-FO gravity solutions constrain the total mass change of Earth for any given month to be zero. The high correlation should be expected from a physical perspective as well—the seasonal amplitudes represent the water exchanged between global ocean and global land (one's gain is the other's loss). The average seasonality of global ocean and global land water mass anomalies are 17.3 ± 0.6 and 17.0 ± 0.6 mm SLE, respectively. The minor differences are due to the additional contributions to the ocean mass from the two ice sheets, and are within the uncertainty range of the two time series.

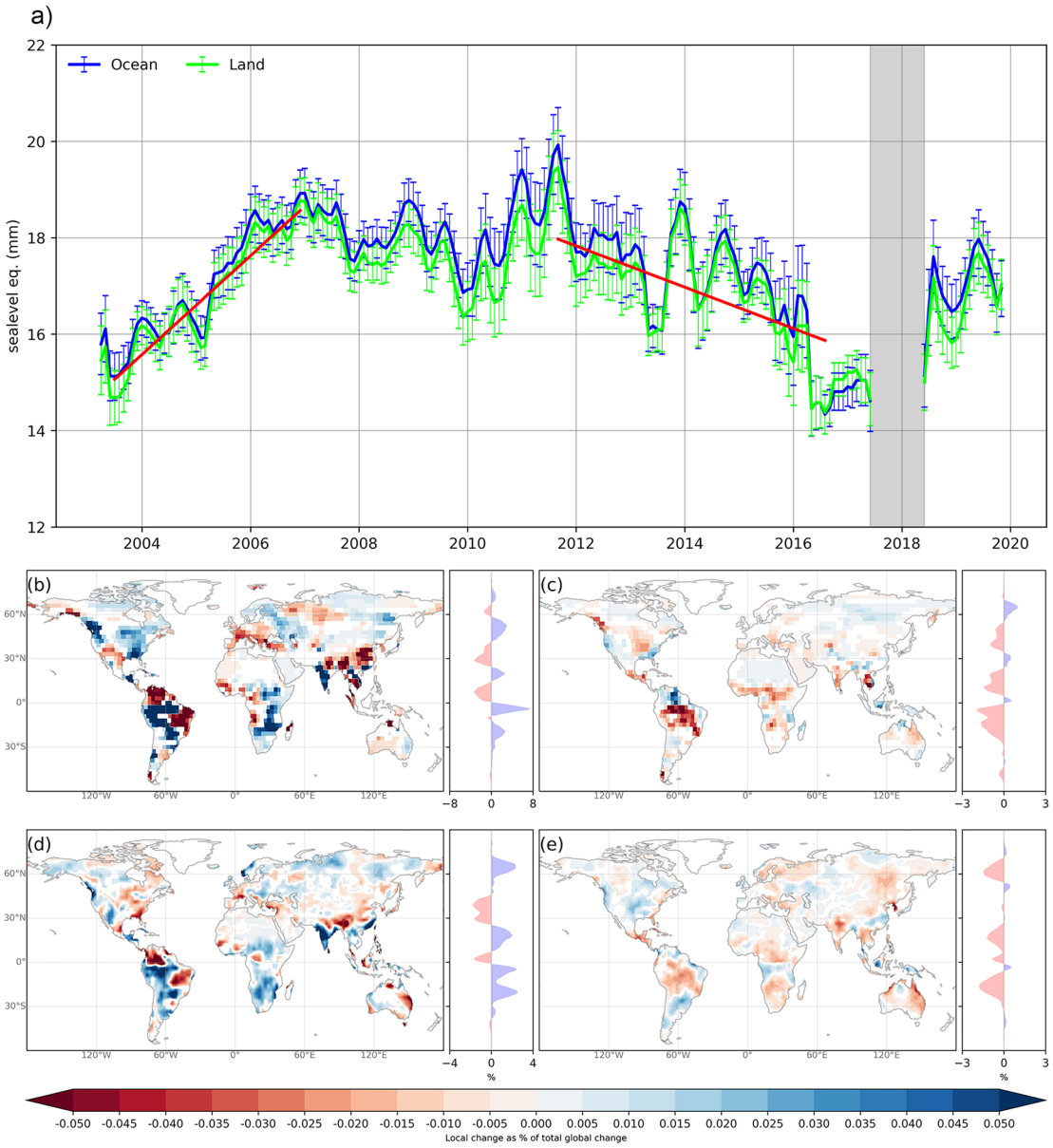

Figure 3. (a) Annual trough-to-peak amplitude fitted over running 2-years sections of GRACE and GRACE-FO global land water (green) and ocean (blue) mass anomalies. Red curves are linear trends highlighting amplification (07/2003–12/2006) and deamplification (09/2011–08/2016). (b and c) Linear trends in local annual trough-to-peak amplitudes over running 2-year sections of GRACE and GRACE-FO land water mass anomalies during the amplification (b) and deamplification (c) periods, respectively. (d and e) Similar trends as (b) and (c), but for GPCP precipitation for the amplification (d) and deamplification (e) periods. The local trends are expressed as % of the total global trend, that is, the sum of the local values is 100%. Only trends significant at 95% confidence interval are considered, after correcting for false discovery rate associated with multiple significance testing. Each map is accompanied by its zonal sum of the local trends on the right, also expressed as a % of total global trend. GPCP, Global Precipitation Climatology Project; GRACE, Gravity Recovery and Climate Experiment; GRACE-FO, GRACE-Follow On.

Since the seasonal global water cycle time series are obtained from spatial integration, understanding which regions contribute to the global seasonal amplitude would help identify regions that are capable of modulating the intensity of the seasonal global water cycle. To investigate the regional controls of global water cycle changes, we focus on land water mass anomalies since water-cycle-related mass fluctuations over the ocean are redistributed very quickly via barotropic waves within a matter of days to a new equal pressure level (Ponte, 2006). Only excess water stored (or lost) regionally on land can explain the observed signals. Since the global ocean and global land water mass time series are statistically indistinguishable from each other

within the uncertainty range, further results describing the seasonal global water cycle (in Section 3.2) focus on global land water mass time series, but we note that those results also apply to global ocean mass time series (within the uncertainty range).

Land water mass anomalies are controlled by local-to-regional hydrology, land-atmosphere interactions, climate, topography, geography, vegetation as well as land use. Figure 2c shows the long-term mean seasonality (trough-to-peak annual amplitude) of water mass anomalies at each land grid point. The regions that show pronounced water exchanges within the year are tropical monsoon regions such as the Amazon basin, tropical Africa, South Asia, and northwest North America. Perennially dry regions at midlatitudes (about 30°) in the northern and southern hemisphere show low seasonality. Similarly, perennially wet regions along the equator such as equatorial Africa and Southeast Asia (Indonesia) also exhibit low seasonality. These findings are consistent with Hamlington et al. (2019), who used cyclostationary empirical orthogonal functions (CSEOF) decomposition of the local terrestrial water storage anomalies to isolate regions that show pronounced seasonality as well as change in seasonal amplitude. However, as we explain further, not all of these high seasonal amplitude regions contribute to the seasonality in global water cycle.

In addition to the amplitude, the regional control of the seasonal global water cycle is also determined by the phasing. As seen in Figure 2d, there are two distinct spatial patterns to seasonal storage peaks. These patterns coincide with seasonal shifts in the intertropical convergence zone (ITCZ) southwards around January and northwards around July, respectively. In the first pattern, due to the ITCZ shift in January, most of the northern hemisphere above 30°N and the southern hemisphere between 0° and 30°S show seasonal storage peaks during February-May. This occurs right after the austral summer monsoon following a 1–3 months lag between precipitation and storage (Hamlington et al., 2019; Humphrey et al., 2016). Over the northern hemisphere, this is after boreal winter and reflects peak snow accumulation. Among these are some of the high seasonal amplitude regions (Figure 2c) such as the Amazon, northwest North America, and tropical southern Africa. Also, extratropical Eurasia, while displaying relatively low local magnitudes, covers a large landmass, and so can be an important contributor when integrated. The second phase pattern is near the tropical northern hemisphere 0–30°N, and beyond 30°S in the southern hemisphere. This aligns with the ITCZ shift toward north (in July) and shows peak storage between July and October, right after boreal summer monsoon, and austral winter snow accumulation. The regions exhibiting this peak storage phase include some high seasonal amplitude regions such as South and East Asia, tropical northern Africa, Orinoco basin, and Central America. It must be noted that seasonal peaking of some regions in South Asia are led by springtime snow mass anomalies in Eurasia (Lin et al., 2020), suggesting an influence of snow-atmosphere coupling in addition to the ICTZ shift.

The key difference between these two spatial patterns is that the storage peaks due to ITCZ southward shift occur over a much larger area than that due to ITCZ northward shift, largely due to a disproportionate land area between northern and southern hemispheres. As a result, when the mass anomalies are integrated across global landmass, the seasonal phasing of the regions corresponding to ITCZ southward shift (i.e., the first pattern from the previous paragraph) prevails, and we see a seasonal peak during around April in the global land water mass anomaly time series (Figure 2a). This is largely driven by the southern tropics (0°–30°S) such as the Amazon, tropical southern Africa, and northern extratropics (30°–90°N), such as northwest North America. This phase difference and disproportionate areas coverage by the two phase patterns is also why the seasonality of the global land and ocean mass (Figure 3a) is distinct from the seasonalities of regional water masses integrated globally (e.g., Figure 1 time series from Hamlington et al., 2019)—depending on the phasing, only certain regions contribute significantly to the net global water cycle. Furthermore, global integration of the regional seasonal amplitudes would also include local moisture recycling that occurs in the land interiors. Thus, this is a case where "the whole is different from the sum of the parts."

3.2. Variations in the Amplitude of the Seasonal Global Water Cycle

The seasonal amplitudes of the global land water mass anomalies (i.e., in the amplitude of the seasonal global water cycle) show a minor long-term linear trend of -0.044 ± 0.017 mm SLE/year that is significant at 95% confidence levels. The seasonal amplitude exhibits pronounced changes from year-to-year and ranges between 14.4 and 19.5 mm SLE (Figure 3a), with the standard deviation of 1.1 mm SLE. Magnitude wise,

the standard deviation is comparable to the long-term linear trends in global land (−0.87 ± 0.06 mm SLE/year) and global ocean (2.02 ± 0.07 mm SLE/year) water mass anomalies.

During 2003–2006 and 2011–2016, there are sustained rapid changes in the seasonal amplitude, signifying an enhancement and a decay in the yearly land-ocean water cycling intensity, respectively. Between 2006 and 2011, the seasonal amplitude is more or less stable (within the uncertainty) and has a significantly higher level than before 2006 or after 2011. From 2016 to 2019, the seasonal amplitude appears to rise up again, though there are 11 consecutive months of missing data during this period. It should be noted that these year-to-year changes in the seasonal amplitude are different from the interannual variability in water mass anomalies. The latter specifically describes changes in the annual mean, whereas the former describes changes in the annual amplitude. They are not dependent on each other, but can cooccur. For example, a climate variability mode could bring about changes in annual amplitude and/or changes in the annual mean.

Next, we examine the periods corresponding with the rapid seasonal amplitude changes, denoted by red trend lines in Figure 3a. Between 07/2003 and 12/2006, the seasonal amplitude of global land water mass increases by 23% (3.9 mm SLE), whereas between 09/2011 and 08/2016, it decreases by as much as 29% (5.0 mm SLE). Both of these changes are significant compared to the uncertainty estimate (±0.6 mm) on the mean amplitude. These periods provide a glimpse of what changes in intensity of the seasonal global water cycle look like. The 07/2003–12/2006 period represents a short-term amplification of the seasonal global water cycle. By the end of the period (12/2006), 3.9 mm SLE more water mass had cycled between the ocean and land than at the start of the period (07/2003). On the other hand, the 09/2011–08/2016 period represents a short-term deamplification of the seasonal global water cycle, with 5.0 mm SLE less water mass cycling between the ocean and land by 08/2016 than it was at the start of the period (09/2011).

We now explore where the largest land changes occurred during the 07/2003–12/2006 global seasonal amplification (Figure 3b) and the 09/2011–08/2016 global seasonal deamplification (Figure 3c). In the figures, the local changes are expressed as % of the total global amplification (or deamplification) signal, that is, the sum of the local values is 100%. We find that 124% of the global amplification signal during 07/2003–12/2006 comes from the southern tropics (0°–30°S), which are dominated by South America (93%) and Africa (45%). Thirty-two percentage of the net global amplification comes from North American midlatitudes (30°–60°N). The rest of the zonal regions show a net decrease in the seasonal amplitude, thereby dampening the global amplification signal. The southern tropics also contributed to the majority (63%) of the deamplification signal during the 09/2011–18/2016 period, led by South America (54%). However, except for Northern high-latitudes (60°–90°N), the rest of the land regions showed deamplification, thus contributing to the global signal to varying degrees. Thus, compared to the 2003–2006 amplification period, when several land regions showed pronounced but opposing amplitude changes, the amplitude changes during 2011–2016 deamplification period were more consistent across regions.

3.3. Potential Drivers of the Changes in the Seasonal Global Water Cycle

Understanding the underlying physical mechanisms involved in such rapid changes in the seasonal global water cycle is an important research topic. Land water storage, being a net residual of terrestrial water balance, can be influenced by the net changes in precipitation, evapotranspiration, and runoff. Understanding changes in the seasonal amplitude of these hydrologic fluxes may help to isolate the causes of rapid variations in water mass seasonality. With complexities in observing global evapotranspiration (e.g., Pascolini-Campbell et al., 2020) and global runoff (e.g., Chandanpurkar et al., 2017), here, we provide a preliminary analysis by examining precipitation seasonality alone. We find that the trends in precipitation seasonality during the two periods (Figure 3d and 3e) generally match the trends seen in seasonality in GRACE water mass anomalies (Figure 3b and 3c). Overall, the southern tropics and northern extratropics explain a similar fraction of the net changes in the amplitude of seasonal precipitation during 07/2003–12/2006 and 09/2011–08/2016 periods, as they do for water storage.

Thus, the changes in the seasonal global water cycle intensity seem to be governed by atmospheric forcings in a few key land regions in the southern tropics and northern extratropics. One of the potential drivers of these changes could be ENSO. Hamlington et al. (2019) showed that ENSO is capable of modulating the seasonal hydrology in certain land regions, some of which (such as the southern tropics) we find contribute

significantly to the global seasonal amplitude (Figure 2c) and its changes (Figure 3b and 3c). However, there are other potential causes outside of climate variability including (but not limited to) external forcing from changes in incoming solar radiation and climate change. These are capable of bringing about changes to ocean precipitation or evaporation, terrestrial water balance, atmospheric capacity for moisture, moisture transport from ocean to land such as driven by changes in land-ocean temperature gradient (i.e., monsoon) or in wind magnitude or direction, cloud and precipitation formation, and land surface characteristics such as albedo and land cover. Examining these drivers, their relative contribution to the global seasonal amplitude, their regional manifestation, hydrologic variables that they influence, and associated feedbacks are topics for future research.

4. Conclusion

In this study, we present the first-ever characterization of year-to-year changes in the seasonal global water cycle. We do so by analyzing GRACE and GRACE-FO data which is unique in its ability to directly measure water mass cycled between global water reservoirs. At seasonal time scales, we find that the global water cycle occurs primarily between global land and global ocean, as the water stored in the atmosphere is negligibly small and the water stored in the ice sheets primarily varies at lower frequencies. The seasonal water mass exchanged between global land and global ocean is about 17.0 $\pm$ 0.6 mm SLE within the year, and is seen to vary significantly from year-to-year with a standard deviation of 1.1 mm SLE. This variability is significant as its magnitude is comparable to the long-term linear trends in global ocean and global land masses. While a minor statistically significant downward long-term linear trend is seen in the amplitude of the seasonal global water cycle, periods of rapid amplification and deamplification by as much as 29% of the mean amplitude, are observed.

Our method directly measures the changes in the water mass cycled between global land and ocean annually, and may be a useful metric to observe climate-driven and climate change-driven intensification of the seasonal global water cycle. The global-scale analysis can be viewed together with seasonal water mass changes at regional scale to identify regions that contribute to the average global amplitude and its changes (amplification and deamplification) and thereby modulate the rate of global intensification. The global signal appears to be driven by land water and precipitation fluctuations over a few key regions, including the southern tropics (0°–30°S, primarily in South America) and the northern extratropics (30°–90°N). Overall, the seasonal hydrology in these regions control the amplitude and phase of the seasonal global water cycle.

Data Availability Statement

GRACE and GPCP data sets used in the study are accessible at https://grace.jpl.nasa.gov/ and https://www.esrl.noaa.gov/, respectively.

Acknowledgments
The research was carried out at the University of California, Irvine, at the Jet Propulsion Laboratory, California Institute of Technology (under a contract with the National Aeronautics and Space Administration), and at the University of Saskatchewan. Funding support of the NASA NEWS program and the GRACE/GRACE-FO Science Team is gratefully acknowledged. J. S. Famiglietti acknowledges research support from the Canada 150 Research Chair program. M.-H. Lo was supported by the grant of MOST 107-2111-M-002-001-MY3.

References

Adler, R. F., Huffman, G. J., Chang, A., Ferraro, R., Xie, P.-P., Janowiak, J., et al. (2003). The version-2 global precipitation climatology project (GPCP) monthly precipitation analysis (1979-present). *Journal of Hydrometeorology*, *4*(6), 1147–1167. https://doi.org/10.1175/1525-7541(2003)004<1147:tvgpcp>2.0.co;2

Benjamini, Y., & Hochberg, Y. (1995). Controlling the false discovery rate: A practical and powerful approach to multiple testing. *Journal of the Royal Statistical Society: Series B (Methodological)*, *57*(1), 289–300. https://doi.org/10.1111/j.2517-6161.1995.tb02031.x

Cazenave, A., Meyssignac, B., Ablain, M., Balmaseda, M., Bamber, J., Barletta, V., et al. (2018). Global sea-level budget 1993-present. *Earth System Science Data*, *10*(3), 1551–1590. https://doi.org/10.5194/essd-10-1551-2018

Chambers, D. P., Cazenave, A., Champollion, N., Dieng, H., Llovel, W., Forsberg, R., et al. (2017). Evaluation of the global mean sea level budget between 1993 and 2014. *Surveys in Geophysics*, *38*(1), 309–327. https://doi.org/10.1007/s10712-016-9381-3

Chandanpurkar, H. A., Reager, J. T., Famiglietti, J. S., & Syed, T. H. (2017). Satellite- and reanalysis-based mass balance estimates of global continental discharge (1993–2015). *Journal of Climate*, *30*(21), 8481–8495. https://doi.org/10.1175/JCLI-D-16-0708.1

Chen, J. L., Wilson, C. R., Chambers, D. P., Nerem, R. S., & Tapley, B. D. (1998). Seasonal global water mass budget and mean sea level variations. *Geophysical Research Letters*, *25*(19), 3555–3558. https://doi.org/10.1029/98GL02754

Dirmeyer, P. A., & Brubaker, K. L. (2007). Characterization of the global hydrologic cycle from a back-trajectory analysis of atmospheric water vapor. *Journal of Hydrometeorology*, *8*(1), 20–37. https://doi.org/10.1175/JHM557.1

Hamlington, B. D., Piecuch, C. G., Reager, J. T., Chandanpurkar, H., Frederikse, T., Nerem, R. S., et al. (2020). Origin of interannual variability in global mean sea level. *Proceedings of the National Academy of Sciences of the United States of America*, *117*(25), 13983–13990. https://doi.org/10.1073/pnas.1922190117

Hamlington, B. D., Reager, J. T., Chandanpurkar, H., & Kim, K. Y. (2019). Amplitude modulation of seasonal variability in terrestrial water storage. *Geophysical Research Letters*, *46*, 4404–4412. https://doi.org/10.1029/2019GL082272

Held, I. M., & Soden, B. J. (2006). Robust responses of the hydrological cycle to global warming. *Journal of Climate*, *19*(21), 5686–5699. https://doi.org/10.1175/JCLI3990.1

Humphrey, V., Gudmundsson, L., & Seneviratne, S. I. (2016). Assessing global water storage variability from GRACE: Trends, seasonal cycle, subseasonal anomalies and extremes. *Surveys in Geophysics*, *37*, 357–395. https://doi.org/10.1007/s10712-016-9367-1

Huntington, T. G. (2006). Evidence for intensification of the global water cycle: Review and synthesis. *Journal of Hydrology*, *319*(1–4), 83–95. https://doi.org/10.1016/j.jhydrol.2005.07.003

Lan, C.-W., Lo, M.-H., Chen, C.-A., & Yu, J.-Y. (2019). The mechanisms behind changes in the seasonality of global precipitation found in reanalysis products and CMIP5 simulations. *Climate Dynamics*, *53*(7–8), 4173–4187. https://doi.org/10.1007/s00382-019-04781-6

Liang, Y.-C., Lo, M.-H., Lan, C.-W., Seo, H., Ummenhofer, C. C., Yeager, S., et al. (2020). Amplified seasonal cycle in hydroclimate over the Amazon river basin and its plume region. *Nature Communications*, *11*(1), 4390. https://doi.org/10.1038/s41467-020-18187-0

Lin, P., Yang, Z. L., Wei, J., Dickinson, R. E., Zhang, Y., & Zhao, L. (2020). Assimilating multi-satellite snow data in ungauged Eurasia improves the simulation accuracy of Asian monsoon seasonal anomalies. *Environmental Research Letters*, *15*(6), 064033. https://doi.org/10.1088/1748-9326/ab80ef

Mouginot, J., Rignot, E., Bjørk, A. A., van den Broeke, M., Millan, R., Morlighem, M., et al. (2019). Forty-six years of Greenland Ice Sheet mass balance from 1972 to 2018. *Proceedings of the National Academy of Sciences of the United States of America*, *116*(19), 9239–9244. https://doi.org/10.1073/pnas.1904242116

Pascolini-Campbell, M. A., Reager, J. T., & Fisher, J. B. (2020). GRACE-based mass conservation as a validation target for basin-scale evapotranspiration in the contiguous United States. *Water Resources Research*, *56*, e2019WR026594. https://doi.org/10.1029/2019WR026594

Peterson, B., Holmes, R., McClelland, J., Vorosmarty, C., Lammers, R., Shiklomanov, I., & Rahmstorf, S. (2002). Increasing river dischange to the Arctic Ocean. *Science*, *298*(13), 2171–2173. https://doi.org/10.1126/science.1077445

Ponte, R. M. (2006). Oceanic response to surface loading effects neglected in volume-conserving models. *Journal of Physical Oceanography*, *36*(3), 426–434. https://doi.org/10.1175/JPO2843.1

Reager, J. T., Gardner, A. S., Famiglietti, J. S., Wiese, D. N., Eicker, A., & Lo, M. H. (2016). A decade of sea level rise slowed by climate-driven hydrology. *Science*, *351*(6274), 699–703. https://doi.org/10.1126/science.aad8386

Shepherd, A., Ivins, E., Rignot, E., Smith, B., Van Den Broeke, M., Velicogna, I., et al. (2018). Mass balance of the Antarctic Ice Sheet from 1992 to 2017. *Nature*, *558*, 211–222. https://doi.org/10.1038/s41586-018-0179-y

Syed, T. H., Famiglietti, J. S., Zlotnicki, V., & Rodell, M. (2007). Contemporary estimates of pan-arctic freshwater discharge from GRACE and reanalysis. *Geophysical Research Letters*, *34*, L19404. https://doi.org/10.1029/2007GL031254

Tapley, B. D., Watkins, M. M., Flechtner, F., Reigber, C., Bettadpur, S., Rodell, M., et al. (2019). Contributions of GRACE to understanding climate change. *Nature Climate Change*, *9*, 358–369. https://doi.org/10.1038/s41558-019-0456-2

Trenberth, K. E., Smith, L., Qian, T., Dai, A., & Fasullo, J. (2007). Estimates of the global water budget and its annual cycle using observational and model data. *Journal of Hydrometeorology*, *8*(4), 758–769. https://doi.org/10.1175/JHM600.1

Velicogna, I., Mohajerani, Y., Geruo, A., Landerer, F., Mouginot, J., Noel, B., et al. (2020). Continuity of ice sheet mass loss in Greenland and Antarctica from the GRACE and GRACE follow-on missions. *Geophysical Research Letters*, *47*, e2020GL087291. https://doi.org/10.1029/2020GL087291

Walter, M. T., Wilks, D. S., Parlange, J.-Y., & Schneider, R. L. (2004). Increasing evapotranspiration from the conterminous United States. *Journal of Hydrometeorology*, *5*(3), 405–408. https://doi.org/10.1175/1525-7541(2004)005<0405:IEFTCU>2.0.CO;2

Watkins, M. M., Wiese, D. N., Yuan, D.-N., Boening, C., & Landerer, F. W. (2015). Improved methods for observing Earth's time variable mass distribution with GRACE using spherical cap mascons. *Journal of Geophysical Research: Solid Earth*, *120*, 2648–2671. https://doi.org/10.1002/2014JB011547

Wiese, D. N., Landerer, F. W., & Watkins, M. M. (2016). Quantifying and reducing leakage errors in the JPL RL05M GRACE mascon solution. *Water Resources Research*, *52*, 7490–7502. https://doi.org/10.1002/2016WR019344

Willis, J. K., Chambers, D. P., & Nerem, R. S. (2008). Assessing the globally averaged sea level budget on seasonal to interannual timescales. *Journal of Geophysical Research*, *113*, C06015. https://doi.org/10.1029/2007JC004517

Wu, W. Y., Lan, C. W., Lo, M. H., Reager, J. T., & Famiglietti, J. S. (2015). Increases in the annual range of soil water storage at northern middle and high latitudes under global warming. *Geophysical Research Letters*, *42*, 3903–3910. https://doi.org/10.1002/2015GL064110